Journal of Materials Chemistry A

PAPER

View Article Online
View Journal | View Issue

Cite this: J. Mater. Chem. A, 2019, 7, 10058

Scalable preparation of hierarchical porous activated carbon/graphene composites for high-performance supercapacitors†

Yilun Huang,[abc] Yunkai Shi,[abc] Qianming Gong,[*abc] Mouyi Weng,[d] Yuyao Li,[abc] Jianning Gan,[abc] Dazhi Wang,[e] Yang Shao,[ac] Ming Zhao,[ac] Daming Zhuang,[abc] Ji Liang,[f] Feng Pan,[*d] Hongwei Zhu[abc] and Cewen Nan[abc]

Received 10th January 2019
Accepted 20th March 2019

DOI: 10.1039/c9ta00353c

rsc.li/materials-a

Hierarchical porous activated carbon particles covered with graphene were prepared by spray-drying a GO/maltodextrin aqueous suspension followed by carbonization and activation. The as-prepared core–shell particles had a high specific surface area (up to 2457 $m^2\ g^{-1}$) and exhibited an outstanding specific capacitance (up to 405 F g^{-1} at 0.2 A g^{-1}, 299 F g^{-1} at 1 A g^{-1} and 199 F g^{-1} at 50 A g^{-1}) along with excellent cycling stability, high energy density and power density in a KOH electrolyte. Moreover, the spontaneous formation of the core–shell structure during the spray-drying process was verified by DFT calculations with the support of XPS chemical analysis and TEM characterization. This designable and controllable strategy of spray-drying could be introduced to design and develop new composite materials with a core–shell structure for potential applications in energy storage, catalysis and adsorption.

Introduction

Supercapacitors are a kind of energy storage device that can be classified as electrical double-layer capacitors (EDLCs) or pseudocapacitors based on their charge storage principles.[1] Limited by their low electrical conductivity, high material cost, poor rate capability, and short working life span, pseudocapacitors are not widely applied in industry. However, EDLCs, which are generally based on the adsorption and desorption of electrolyte ions on the surface of porous electrode materials, have a high power density, rapid charging process, and long life span. Since EDLCs have the advantages of both dielectric capacitors and batteries, an increasing number of researchers have focused on developing novel and high-performance electrode materials for EDLCs using conventional activated carbon (AC) with emerging graphene or graphene-based carbon materials.[2,3] Conventional AC materials have been extensively used as the main electrode materials for supercapacitors due to their low production cost and acceptable performance. However, AC has some disadvantages, such as non-optimized pore size and distribution, low electrical conductivity, and limited electrochemical capacitance.[3–5] Therefore, with the development of energy storage market needs and fierce competition from other kinds of energy storage devices, such as lithium ion batteries, advanced electrode materials other than AC are expected to exhibit higher capacitance and rate capability with better stability.

Recently, graphene and its derivatives have been preferentially used for supercapacitor electrode materials due to their special sp^2-hybridized carbon atoms, high specific surface area, tunable pore structure, and high intrinsic electronic mobility.[6–9] Generally, there are two main strategies to prepare graphene-based electrodes for supercapacitors. One is to use graphene as the electrode material; for instance, activated graphene aerogel[10] and three-dimensional graphene spheres[11] have been prepared as electrode materials, and they exhibited good capacitive performances. Since graphene is difficult to fabricate on a large scale at low cost, another strategy is to make graphene-based composites by combining graphene with metal–organic frameworks, metallic oxides/hydroxides, polymers, or other carbon materials.[6–8,12] Graphene composites with non-carbon materials are used in faradaic pseudocapacitors, while graphene/carbon composites are more attractive for use in EDLCs. For example, porous graphene/AC composites can be obtained by simply mixing graphene and a carbon precursor in water or an organic solvent in a hydrothermal reactor followed by heat treatment or alkali activation. In most cases, this kind of

[a]School of Materials Science and Engineering, Tsinghua University, Beijing 100084, People's Republic of China. E-mail: gongqianming@mail.tsinghua.edu.cn
[b]State Key Laboratory of New Ceramics and Fine Processing, Tsinghua University, Beijing 100084, People's Republic of China
[c]Key Laboratory for Advanced Materials Processing Technology, Ministry of Education, Beijing 100084, People's Republic of China
[d]School of Advanced Materials, Shenzhen Graduate School, Peking University, Shenzhen 518055, People's Republic of China. E-mail: panfeng@pkusz.edu.cn
[e]Beijing HCC Energy Technology Co., Ltd, Beijing 100085, People's Republic of China
[f]Department of Mechanical Engineering, Tsinghua University, Beijing 100084, People's Republic of China

† Electronic supplementary information (ESI) available: Additional experimental details of material preparation and characterization. See DOI: 10.1039/c9ta00353c

electrode material demonstrates high rate and high capacitance performance with a gravimetric capacitance of 200–350 F g^{-1} in aqueous electrolytes.[11,13] Previous research has shown that ideal electrode materials for supercapacitors should have a high specific surface area, desirable pore size with a suitable distribution, which allows efficient diffusion of ions from the electrolyte to the inner zone of the electrodes, and low electrical resistance, which is beneficial for the rate capability.

In this work, we demonstrated a scalable synthesis of core–shell graphene-covered AC by spray-drying a maltodextrin/GO aqueous suspension followed by carbonization and activation of the maltodextrin@GO composite particles. We have acquired excellent capacitance properties and outstanding cycling stability based on the hierarchical porous carbon material. More than that, we have found a good material preparation strategy with good designability and controllability based on theoretical analyses and experimental verification. For example, in this strategy, graphene was adopted as the shell to improve both the electrical conductivity and pore structure stability of the composite particles. Moreover, the flexible graphene shell could be modified to be thick or thin, porous or closed, or even multi-shelled by repeating the spray drying process. Further, with the help of DFT calculations, XPS chemical analysis and TEM characterization, the formation mechanism of the core–shell structure was verified. The designability of this technology might help to develop new core–shell composite materials with a tunable pore structure and electrical conductivity by combining graphene and other materials. The composite particles with graphene or other 2D materials as the shell might be useful as energy storage materials, catalytic materials or adsorption materials based on the published papers about core–shell carbon materials.

Results and discussion

Fig. 1 shows the fabrication process of graphene-covered AC *via* the spray-drying technique followed by carbonization and alkali-activation procedures. First, GO and maltodextrin were well dispersed in water in different proportions (m_{GO} : (m_{GO} + $m_{maltdextrin}$) = 5 wt% and 10 wt%), and this slurry-like mixture was fed using a peristaltic pump into a preheated spray-drying machine (Fig. 1a). Subsequently, the compressed air carrying the feedstock was sprayed out through a porous nozzle to create discrete atomized suspension drops of the slurry. As these drops fell, they were rapidly heated at high temperature (~140 °C) in a cylindrical drying chamber. Since water evaporated during the rapid drying process, dried powders coated with wrinkled GO were obtained.[14] Then, these powders were further carbonized and activated using an alkali. Finally, porous, core–shell reduced GO (rGO)/AC particles were acquired (Fig. 1b). The core–shell structure of the rGO/AC composite materials was examined in detail by transmission electron microscopy (TEM) and scanning electron microscopy (SEM), and the formation mechanism was further explored by density functional theory (DFT) calculations and is discussed in the next section.

The intermediate GO/maltodextrin particles obtained by spray drying and the final rGO/AC particles were characterized by SEM and TEM. Fig. 2a shows the spray-dried GO/maltodextrin particles (GMP-5) from the suspension (m_{GO} : (m_{GO} + $m_{maltdextrin}$) = 5 wt%). The particles were approximately 2–20 μm in diameter, and distinct wrinkles can be seen on the surface of these micron-sized particles, which are translucent in the TEM field (Fig. 2e) of view for they are composed of a thin GO shell and an organic maltodextrin core

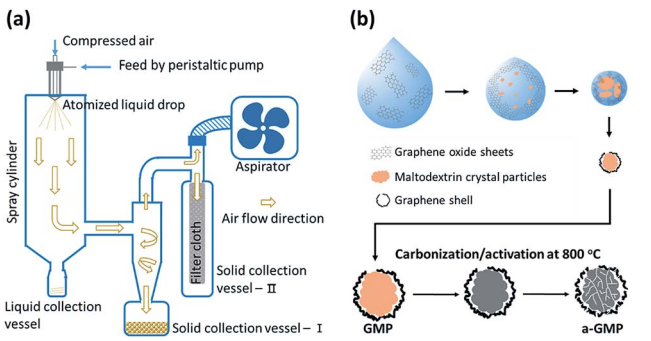

Fig. 1 Scheme of the fabrication of a-GMP by a spray-drying method. (a) Schematic drawings illustrating the spray-drying process. (b) Proposed mechanism of the transformation of GO sheets and maltodextrin into a-GMP by a spray-drying method and subsequent carbonization and activation processes.

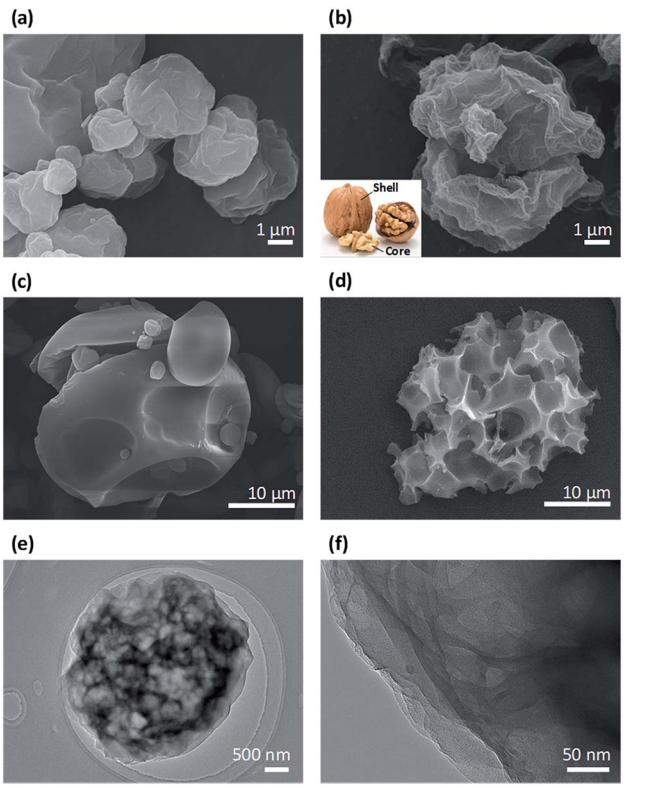

Fig. 2 SEM images of (a) mixed GO and maltodextrin powder (GMP) and (c) pure maltodextrin powder (MP) prepared by the spray-drying method and their carbonized and activated products: (b) a-GMP and (d) a-MP. The insert in (b) is a digital photograph of walnuts with hard, wrinkled shells covering an inner core. (e and f) TEM images of GMP.

(Fig. 2f). Compared with the smooth surface of the pure maltodextrin powder (MP) produced by the same spray-drying process shown in Fig. 2c, the wrinkles on the surface of GMP-5 can be attributed to the GO added to the suspension. Thus, increasing the amount of GO (from 5 wt% to 10 wt% or 100 wt%) should result in more wrinkles on the surface (Fig. S1†). However, the composition of the wrinkles, *i.e.*, GO or maltodextrin or a mixture of both, has yet to be determined. Fig. 2b and d show the SEM images of GMP-5 and pure MP after the carbonization and activation processes. It can be seen that the activated GMP-5 (a-GMP-5) keeps a core–shell structure and the wrinkles on the surface of a-GMP-5 were more evident than those on the original GMP-5. In contrast, the activated MPs (a-MPs) show different microstructures with dotted pits on the surface, and these pits are the result of molten potassium hydroxide (KOH) etching at a high temperature of 800 °C. To determine the variation of the core–shell structure from pristine GMP to a-GMP, more SEM and TEM results are provided in Fig. S2–S4.† The morphology of spray-dried GO/maltodextrin particles (GMP-10) from the suspension ($m_{GO} : (m_{GO} + m_{maltdextrin}) = 10$ wt%) is similar to that of GMP-5 in Fig. S2.† After being carbonized and activated, the surface morphology changed gradually. Since the carbon yield of maltodextrin was only approximately 20 wt%,[15] the spheres shrank and some zones collapsed inward, so the surface became rough especially after being activated (Fig. S3†). The wrinkled surface layer in carbonized GMP-10 (c-GMP-10) should be the reduced GO (rGO) shell according to TEM observations (Fig. S4a–c†), while after activation, the rough surface turned into a flower-like morphology (Fig. S2c and d†) and consequentially, the continuous shell turned into a scale-like porous structure in a-GMP-10 (Fig. S4d–f†). All the SEM and TEM observations could qualitatively demonstrate the hierarchical pore structure of spherical a-GMP. The relatively thick core is surrounded by a rGO shell. The rGO/AC core–shell structure probably originated from the spray-drying process during which maltodextrin crystallized and potentially adsorbed GO. The evaporation of water caused the GO to wrinkle, and a porous GO "shell" was *in situ* constructed. In addition, theoretical analyses with DFT calculations were used to further probe the formation mechanism of this core–shell structure accompanied with experimental verification in the following section. Since the maltodextrin-derived AC was protected by the rGO "shell", the pore structure was more stable during charge/discharge cycling when the core–shell composite was applied as the electrode material for supercapacitors.

X-ray diffraction (XRD) and Raman spectroscopy are important methods for analysing the defects and crystallinity of carbon materials. The XRD patterns of the pristine and as-prepared materials are shown in Fig. 3a. The results show that pure MP has a broad peak at approximately 18° and the GO powder exhibits a sharp peak at approximately 11°, which is the characteristic peak of GO (001).[16] After the subsequent carbonization and activation steps at 800 °C, the peaks of maltodextrin at 18° and GO at 11° disappeared in the patterns of a-MP, a-GMP-5, and a-GMP-10. However, a new broad peak appeared at approximately 26° in the patterns of the a-GMP-5 and a-GMP-10 samples, which is a characteristic peak of the (002) plane of graphite. This variation in the peaks demonstrates that maltodextrin becomes amorphous carbon and GO is reduced to graphene. In addition, the 26° peak in the a-GMP-10 pattern is sharper than that of the other two samples, which might be due to the higher ratio of GO added. Since a higher degree of crystallinity can lead to carbon materials with enhanced electrical conductivity,[17] the a-GMP-10 sample is expected to have a lower inter-resistance, as verified by electrochemical tests in the following section. The Raman spectra of the activated samples are shown in Fig. 3b. In general, all samples show similar G peaks at 1590 cm^{-1}, correlating with the in-plane size of the (002) crystal plane, and D peaks at 1350 cm^{-1}, denoting lattice distortions and other defects. It should be noted that a-GMP-5 and a-GMP-10 exhibit D′ peaks at approximately 2700 cm^{-1}, which indicates the presence of rGO.

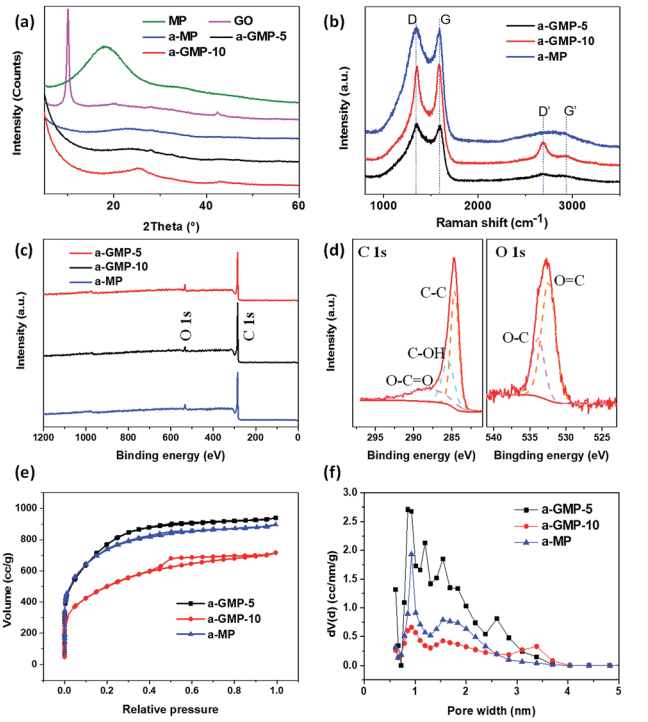

Fig. 3 (a) XRD patterns of the raw materials and the as-obtained samples. (b) Raman spectra of a-GMP-5, a-GMP-10, and a-MP with Raman shifts from 800 to 3500 cm^{-1}. (c) XPS survey spectra of the elemental composition of the as-produced samples (a-GMP-5, a-GMP-10 and a-MP). (d) High resolution C 1s and O 1s XPS spectra of a-GMP-5. (e) N_2 adsorption/desorption isotherms and (f) QSDFT differential pore-size distributions.

The ratio of the elements, the bonding configurations and chemical coordination states can be determined by XPS. The XPS survey spectra in Fig. 3c and S5† indicate that the samples are mainly composed of C and O elements, which are listed in Table S1.† The carbonization and activation processes led to the variation of the O element, *i.e.*, decreasing from approximately 40 at% to 5.77, 3.51 and 4.87 at% for a-GMP-5, a-GMP-10 and a-MP, respectively. The high resolution C 1s XPS spectra in Fig. 3d, S6a and b† can be deconvoluted into three peaks corresponding to C–C sp^2 (284.5 eV), C–OH (285.9 eV), and O–C=O

(288.2 eV), respectively.[18] Fig. 3d, S6c and d† show the high resolution O 1s XPS spectra which can be deconvoluted into two peaks of O=C (532.4 eV) and O–C (534.5 eV) indicating the presence of carbon–oxygen functional groups on the surface of carbonized and activated samples.[19] These oxygen-containing functional groups that are mainly located at defective sites could contribute to pseudocapacitance to some degree when the as-prepared carbon materials (a-GMP-5, a-GMP-10 and a-MP) are applied as electrode materials for supercapacitors. Meanwhile, the oxygen-containing groups could do good to the wettability of carbon materials as well as providing additional active sites for electrolyte ions.[20,21] Thus, a-GMP-5 with a higher oxygen content and suitable carbon–oxygen coordination states exhibited a better capacitive performance.

The XRD, Raman and XPS results are consistent with the SEM observations that the as-prepared porous samples are composed of rGO and maltodextrin-derived carbon. The capacitive performances of supercapacitors are mainly determined by the pore structure and electrical conductivity of the electrode materials; thus, the as-prepared porous rGO/AC particles are expected to be good electrode materials for supercapacitors. Fig. 4a presents the cyclic voltammetry (CV) curves of a-GMP-5 in a three-electrode cell with 6 M KOH as the electrolyte. The rectangular-shaped voltage–current curves in the range of −1 to 0 V at scan rates ranging from 5 to 100 mV s^{-1} are exactly consistent with those of EDLCs with AC electrodes. The electrochemical performances were further examined by electrochemical impedance spectroscopy (EIS) analysis to distinguish the electric conductivity of the working electrode material. The equivalent circuit model is shown in Fig. S7,† which helps to describe the experimental results.[22] All samples exhibit Nyquist plots with similar shapes consisting of a small semicircle and a straight line (Fig. 4b). The semicircle denotes the interface resistance of the working electrode, and the intercept at the Z' axis is considered the equivalent series resistance (ESR).[11,23] The ESR values of a-GMP-5, a-GMP-10 and a-MP are 0.53, 0.40 and 0.56 Ω, respectively. The decline in the ESR with the addition of 5 wt% GO is not remarkable, but the charge transfer resistance (R_{ct}) of a-GMP-5 (0.21 Ω), denoted by the radius of the semicircle in the Nyquist plot, is much lower than that of a-MP (0.50 Ω). The R_{ct} value of a-GMP-10 (0.23 Ω) is similar to that of a-GMP-5. Thus, 10 wt% GO can improve the conductivity of the electrode by decreasing the charge transfer resistance and ESR. The detailed results can be seen in Table S2.†

A galvanostatic charge–discharge (GCD) test was used to characterize the capacitive behaviours of the samples (Fig. 4c and d). The specific capacitance of a supercapacitor is a function of the charge–discharge current density, which decreases with an increase in current density in the range of 1 to 100 A g^{-1} due to limited ion diffusion in the electrode and higher internal impedance at high current densities. The electrode with graphene-covered AC (a-GMP-5) exhibits higher specific capacitances (up to 405 F g^{-1} at 0.2 A g^{-1}) than a-MP and commercial AC (Fig. 4e). Meanwhile, a-GMP-5 exhibits good rate capability and specific capacitances at 1 and 50 A g^{-1} are 299 and 199 F g^{-1}, respectively. This enhancement can be attributed to the large specific surface area and hierarchical porous structure of the sample and will be analysed in the next section. A comparison of the capacitive performances in this work with those of other graphene-based materials for supercapacitors in aqueous electrolytes is shown in Table S3.†[10,11,24–29] Although the specific capacitance of a-GMP-5 is a little inferior to that of the ones synthesized by Yin *et al.*[26] (318 F g^{-1} at 1 A g^{-1}), when considering the scalability and designability of the strategy in this work, we suppose a-GMP-5 would be a promising electrode material for supercapacitors. The average coulombic efficiency of a-GMP-5 at a current density of 0.2 A g^{-1} is 93.26% and with the current density increasing, the coulombic efficiency increased to 99.63% at a current density of 20 A g^{-1}. The

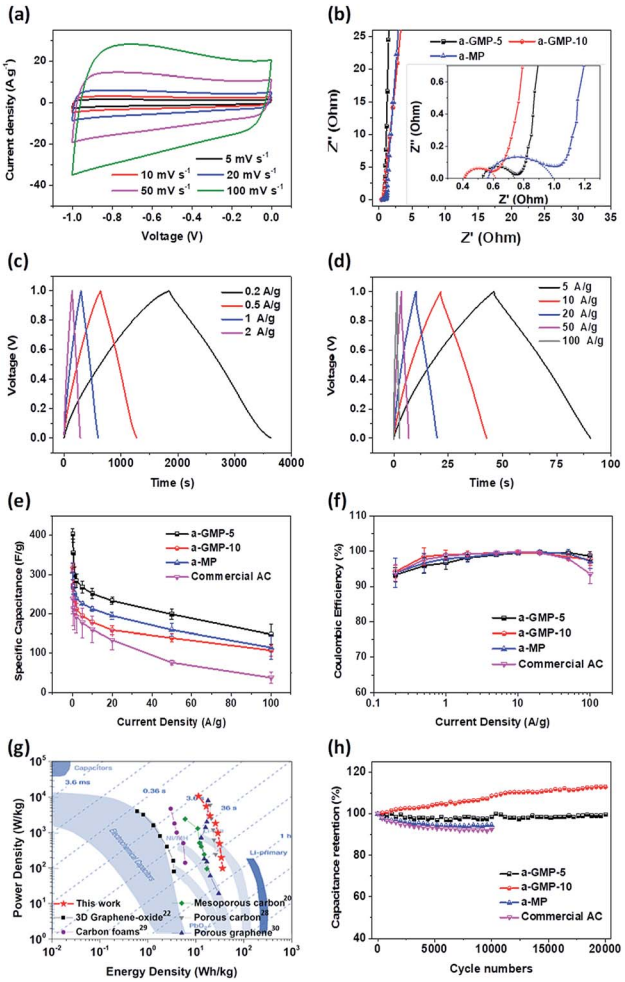

Fig. 4 (a) CV curves for a-GMP-5 at different scan rates from 5 to 100 mV s^{-1}. (b) Nyquist plots in the frequency range from 100 kHz to 10 mHz; the inset shows the enlarged plot at high frequency. (c and d) GCD curves of a-GMP-5 obtained at different current densities from 0.2 to 100 A g^{-1}. (e) Specific capacitances of the as-obtained samples and commercial AC at different current densities from 0.2 to 100 A g^{-1}, which were measured from GCD curves. (f) Coulombic efficiencies of the as-prepared samples and commercial AC at different current densities from 0.2 to 100 A g^{-1}. (g) Ragone plot of the specific gravimetric energy density and power density of the as-prepared a-GMP-5 sample in comparison with those of common energy storage devices and carbon-based materials. (h) Cycling performance at a current density of 50 A g^{-1}.

coulombic efficiency results of the as-prepared samples and commercial AC are shown in Fig. 4f. In addition to being tested in a typical three-electrode cell, a-GMP-5 was also examined as the electrode material in two-electrode supercapacitor cells and it demonstrated a higher specific energy density (36 W h kg^{-1} at a current density of 0.2 A g^{-1}) and power density (11 kW kg^{-1} at a current density of 50 A g^{-1}) than common electrochemical capacitors and some carbon-based materials (Fig. 4g).[20,22,29–32] The details of the energy density and power density calculations can be seen in the ESI and Fig. S8.† However, the a-GMP-10 sample, with a higher graphene content, did not show a higher specific capacitance than a-MP, indicating that the thick graphene shell covering the AC core might block micropores or diffusion channels, which would negatively affect ion diffusion.

Cycling stability is a crucial parameter for practical applications of supercapacitors. The long-term cycling stability was evaluated by repeating the GCD test between 0 and 1 V at a current density of 50 A g^{-1}. Fig. 4h shows the relationship between the capacitance retention and cycle number. After 10 000 cycles, the residual capacitances of a-MP and commercial AC are 94.6% and 92.5%, respectively, which are not acceptable for industrial applications. In contrast, for the a-GMP-5 and a-GMP-10 samples after 20 000 cycles, the capacitance retention is 99.5% and 113.0%, respectively. The excellent cycling performances of these two as-obtained samples can be reasonably attributed to the rGO shell, which can prevent the micropore structure from collapsing and improve the electrical conductivity. Degradation of the porous structure is the main reason for supercapacitor ageing.[33] However, the structure of the a-GMP-5 sample after the cycling test remained stable, which could be verified by SEM and BET analyses in Fig. S9, S10 and Table S4.† In particular, the abnormal increase in the capacitance of a-GMP-10 should be further investigated in future work. Interestingly, this phenomenon was also reported in some previous studies.[20,21,34,35] One acceptable explanation of this phenomenon might be that there is an activation process in the electrode material during cycling. Such an activation process presumably originates from the enhancement of electrolyte infiltration and the disclosing of an additional surface area by the repeated charging and discharging.[20] Particularly, it has been reported that graphene is hydrophobic[36–38] and the aqueous electrolyte infiltration or diffusion into the graphene-covered a-GMP-10 sample might not be that smooth at the beginning, and in addition, the a-GMP-10 sample has less micropores than the other two samples (a-GMP-5 and a-MP), so the cyclic charge and discharge would not only presumably help to improve the electrolyte wettability but also increase the micropore volume in the sample according to published work. Correspondingly, this activation would promote the specific capacitance along with the cyclic tests.

BET analysis and DFT calculations can provide more information about the formation mechanism of the shell-like structure and enhanced capacitive performance with the addition of GO. The pore structure of an electrode material is a critical factor affecting the electrochemical performance of a supercapacitor. Herein, Brunauer–Emmett–Teller (BET) and quenched solid density functional theory (QSDFT) models have been used to determine the specific area and pore size distribution of the samples.[39,40] Basic pore structure information was obtained through N_2 adsorption/desorption tests, and the results are shown in Fig. 3e and Table 1. All samples have similar adsorption/desorption isotherms typical of AC materials, indicating that the pores should be mostly micropores according to the IUPAC isotherm classification system.[41,42] In particular, the specific surface area of a-GMP-5 is 2457 m^2 g^{-1}, which is 1.8 times more that of commercial AC materials and higher than that of the other as-prepared samples. In comparison, a-GMP-10 has the lowest specific surface area of 1401 m^2 g^{-1}, which indicates that adding an excess of GO to maltodextrin might have negative side effects on micropore formation because a thicker rGO shell results in less activation by KOH at 800 °C due to its high stability.[23] The pore structure of a-GMP-10 is in accordance with its lower specific capacitance determined by CV and GCD tests relative to that of the other rGO shell samples. Meanwhile, according to the pore size distribution (PSD) curves in Fig. 3d, the micropore and mesopore sizes range from 0.6 to 5 nm for a-GMP-5, a-GMP-10 and a-MP, as determined by the QSDFT method. It can be seen that a-MP has a narrow peak when the pore width < ~2 nm, which indicates that the sample has a narrow distribution of micropores. However, a-GMP-5 exhibits a main peak at approximately 1 nm accompanied by several small peaks ranging from 1 to 4 nm, indicating a hierarchical porous structure. As for a-GMP-10, although the pore distributions of a-GMP-10 and a-GMP-5 are similar, the micropore volume is much lower for a-GMP-10. The PSD results indicate that the samples with GO added to the raw material exhibit hierarchical pores with a size distribution from 0.6–4 nm, while no such pores appeared in the a-MP samples. The mesopores probably come from the shell layer based on the SEM observations (Fig. 2b). The electrical double layer principle of supercapacitors predicts that the capacitive performance of electrode materials with highly developed hierarchical porous structures would be much better than that of materials with uniform micropores.

If the formation of the rGO core–shell structure can be corroborated by theoretical analyses, mass production of the electrode material *via* this spray-drying technology could be possible. In this study, DFT calculations[43] were adopted to explore the formation process of a core–shell structure with graphene and maltose as the study subjects, because they most closely match the experimental materials. The calculation systems included a single maltose molecule (Fig. 5a),

Table 1 BET specific surface areas of the as-obtained samples and commercial AC

Samples	BET specific surface area (m^2 g^{-1})
a-GMP-10	1401
a-GMP-5	2457
a-MP	2278
Commercial AC	1374

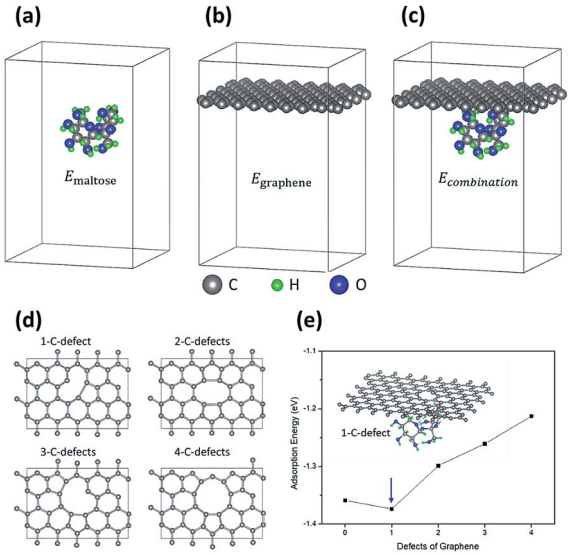

Fig. 5 The structure of (a) maltose, (b) graphene, and (c) graphene combined with maltose. (d) Snapshots of initial graphene defects. (e) The adsorption energy of the defective graphene/maltose system with different numbers of C defects in graphene.

a graphene layer (Fig. 5b), and a combined maltose molecule and graphene sheet (Fig. 5c).

In our calculation, we found that the adsorption energy between a no-defect single layer of graphene and a maltose molecule is −1.359 eV in a water system.[44] The negative energy means that the system can achieve a more thermodynamically stable state when graphene is adsorbed onto the surface of maltose.[45] In other words, the DFT calculation results indicate that graphene adsorption onto maltose molecules or crystals during the spray-drying process is spontaneous and inevitable. Since GO has a higher polarity than graphene, the adsorption energy between GO (or defective graphene) and maltose molecules should be different.[46] Herein, we introduced vacancy defects in graphene to simulate GO. Some typical graphene vacancy defects were selected for the calculations, and the results are shown in Fig. 5d.[47–49] The defects included monovacancies and pentagonal or heptagonal rings by removing one to four carbon atoms. The adsorption energy of the defective graphene/maltose systems obtained from DFT calculations is shown in Fig. 5e, and a transition can be observed with a one carbon atom vacancy. The $E_{adsorption}$ value first decreased to −1.374 eV and then increased to −1.213 eV with four carbon atom defects, which implied that only specific graphene defects can increase the probability of graphene and maltose combination; however, adsorption will occur regardless of whether the graphene sheet is non-defective or defective. We also probed the adsorption energy of other carbon precursors, such as glucose and graphene (Fig. S11†). The DFT calculations produced similar results, showing that glucose molecules and graphene sheets can self-assemble due to the $E_{adsorption}$ of graphene/glucose, −1.528 eV. Meanwhile, additional chemical analyses with XPS were employed to further ascertain the formation of core–shell structures (Fig. 6). Generally, GO prepared by Hummers' method will inevitably contain some

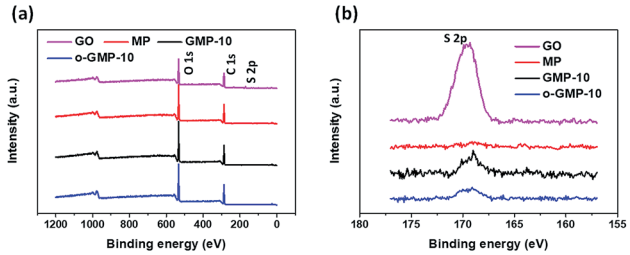

Fig. 6 (a) XPS survey spectra of the elemental composition of GO, MP, GMP-10 and o-GMP-10. (b) High resolution S 2p XPS spectra of the samples.

residual sulphur content,[50] which could be a marker in XPS analyses. In addition, to make a comparison between the as-prepared core–shell structure of GMP and the random mixture of GO and maltodextrin, we made a control sample of oven-dried GO/maltodextrin (ratio of GO was 10 wt%) from an aqueous suspension (o-GMP-10). In Fig. 6a, all four samples show similar XPS survey spectra, except GO with a small peak of S 2p at a binding energy of 169.5 eV.[20,51] The high resolution S 2p XPS spectra shown in Fig. 6b demonstrate the different intensities of these samples and the detailed atomic concentrations of the samples are listed in Table S5.† It is clear that the S content in GMP-10 is much higher than that in o-GMP-10. Considering the limited detection depth of XPS (≤∼10 nm) (Fig. S12†),[52] we can confirm that the chemical composition acquired by XPS should be just the constituents of the surface layer or the shell. Comparing the S contents of MP, GMP-10 and o-GMP-10 in Table S5,† we can infer that GMP-10 should be covered with a thin layer of GO and in contrast, no or few core–shell structures were produced during oven-drying of the GO/maltodextrin suspension. The influence of the distribution of GO in GO/maltodextrin particles on XPS tests is illustrated in Fig. S12† and the quantitative chemical analyses are also in good agreement with the supposed core–shell structure.

Although SEM, TEM and XPS analyses support the assumption of the core–shell structure which was further verified by DFT calculations during the spray-drying process, there might be some random mixture of GO and maltodextrin as well because of the dynamic and pulsed spray-drying process. In brief, as shown in Fig. 1b, during the spray-drying process, the GO and maltodextrin molecules dispersed in small aqueous drops spontaneously combine, and due to the self-assembly of graphene into wrinkled graphene films,[53–55] core–shell graphene-covered carbon composites were successfully prepared. More encouragingly, the core–shell structure could be maintained after the subsequent carbonization and activation processes, so the excellent cycling performance of the supercapacitor samples with rGO/AC as the electrode material could be guaranteed.

Experimental

Materials

GO powder used in this work was obtained by a modified Hummers' method.[50] 4–17 DE maltodextrin was purchased

from Cool Seoul Bio. All other chemicals, including hydrochloric acid, ethanol, and potassium hydroxide, were purchased from Peking Reagent. All chemicals were used as received. The procedure for the fabrication of a-GMP is illustrated in Fig. 1, including two main steps in sequence: (1) preparation of GMP by a spray-drying method and (2) carbonization and alkali-activation processes.

Mixing and spray drying

First, 0.2 g/0.4 g (for GMP-5/GMP-10) GO powder was added to 76 g DI water and dispersed by ultrasonication with a power of 80 W for 1 h. Then, 3.8 g/3.6 g (for GMP-5/GMP-10) maltodextrin powder was added to obtain a solution with a 5% solid content that was sonicated for another 1 h. In addition, 4 g maltodextrin powder without GO was added to 76 g DI water and dispersed by ultrasonication to prepare pure MP. Next, this aqueous GO/maltodextrin solution was fed into a spray dryer (Buchi 290 mini spray dryer) using a peristaltic pump. The inlet air temperature was 160 °C, and the atomizer pressure was 50 psi. During this process, atomized liquid drops were produced. The droplets were carried from the spray cylinder to a cyclone separator and dried in hot air to produce micron-sized particles. These particles were collected in two solid collection vessels. This spray-drying method yielded GMPs and MPs.

Carbonization and alkali-activation processes

GMP and MP were placed in a corundum boat in a tube furnace, heated to 300 °C and held at that temperature for 1 h in an argon (Ar) atmosphere. According to the thermogravimetric curve of maltodextrin, the maltodextrin weight loss rate was highest at 300 °C. After this step, maltodextrin was carbonized, and graphene was heat reduced. Then, the intermediate products were mixed with KOH at a weight ratio of 1 : 4. This mixture was heated to 800 °C in a tube furnace in an Ar atmosphere. The heating protocol was as follows: (i) heating to 400 °C at a rate of 10 °C min^{-1} and holding for 0.5 h to melt KOH and thoroughly mix the sample; (ii) heating to 800 °C at a rate of 5 °C min^{-1} and holding for 1 h to obtain alkali-activated materials; and (iii) cooling to room temperature. The obtained sample was washed with 1 mol L^{-1} HCl to remove excess alkali and then washed with DI water to achieve a neutral pH. After vacuum drying at 120 °C for 12 h, the a-GMP and a-MP samples were obtained.

Characterization

Scanning electron microscopy (SEM) images were collected on a JSM-7001F field emission scanning electron microscope, and transmission electron microscopy (TEM, Tecnai G20) was used to obtain the microcosmic structure and morphology of the samples. The phase composition and the degree of crystallinity were identified by X-ray diffraction (XRD, D/max-2550) measurements. The N_2 adsorption/desorption isotherms were measured at 77 K on a Micromeritics ASAP 2020 instrument. The specific surface area was measured by the Brunauer–Emmett–Teller (BET) method. The pore size distributions ranging from 0.6 to 5 nm were determined by the QSDFT method. Raman spectroscopy was performed on a HORIBA LabRAM HR Evolution spectrometer. X-ray photoelectron spectroscopy (XPS) analyses were carried out on a PHI Quantera SXM with a monochromatic Al Kα X-ray source.

Electrochemical measurements

An aqueous three-electrode setup was used for single-electrode characterization. The as-obtained samples were mixed with a PTFE binder and BLACK PEARLS 2000 carbon black conductor at a weight ratio of 8 : 1 : 1. Then, the mixture was coated on a 1 cm^2 Ni foam substrate and used as the working electrode. A 1 cm^2 Pt sheet was used as the counter electrode, and a saturated calomel electrode (SCE) electrode was used as the reference electrode. The electrolyte was 6 M KOH. The amount of the active material loaded in the electrode is shown in Table S6.† Cyclic voltammetry (CV) and electrochemical impedance spectroscopy (EIS) analyses were performed on a Biologic SAS VSP-300 electrochemical workstation. Galvanostatic charge–discharge (GCD) and cyclical tests were performed on an Arbin supercapacitor testing system.

DFT calculations

DFT calculations were performed on graphic processing unit (GPU) processors in the PWmat code.[56,57] To simulate the adsorption process, we first calculated the adsorption energy of maltose molecules on graphene. We performed atom relaxation to ensure that the residual force on each atom was less than 0.01 eV $Å^{-1}$ for the following systems: a single maltose molecule (Fig. 5a), a graphene layer (Fig. 5b), and a combined maltose molecule and graphene sheet (Fig. 5c). In these structures, we used a lattice constant of 17.04 Å × 19.68 Å × 30.00 Å to ensure that the vacuum layer along the *c* axis was long enough for the graphene sheet or the combined couple. In addition, this set of lattice constants ensures that the vacuum layer along the *a* and *b* axes is thick enough for the maltose molecule calculation. During our calculation, the van der Waals interaction was corrected by the DFT-D2 method.[58] A Monkhorst–Pack grid[59] was used in our process of *K*-point sampling. For the graphene sheet and combined system, a set of 4 × 4 × 1 *K*-points was used with a total test energy error of approximately 1 meV. For the maltose molecule calculation, a set of 1 × 1 × 1 *K*-points was used. The SG15 pseudopotential[60,61] with a cut-off energy of approximately 810 eV was used in our calculation. We used the following formula to calculate the adsorption energy.

$$E_{\text{adsorption}} = E_{\text{combination}} - E_{\text{maltose}} - E_{\text{graphene}}$$

where $E_{\text{combination}}$ is the energy of the system combining a maltose molecule with graphene, E_{maltose} is the energy of a maltose molecule, E_{graphene} is the energy of a graphene sheet and $E_{\text{adsorption}}$ is calculated by subtraction.

Conclusions

In this work, we have demonstrated a scalable synthesis strategy for preparing porous AC particles covered with rGO by spray-drying an aqueous suspension of GO/maltodextrin followed by

carbonization and activation processes. The as-prepared a-GMP particles were composed of wrinkled rGO shells and AC cores. This unique AC@rGO structure was beneficial for improving the conductivity, electrolyte ion diffusion efficiency and pore structure stability when the composite particles are used as electrode materials in supercapacitors. The a-GMP-5 samples exhibited a high specific capacitance of 405 F g^{-1} at 0.2 A g^{-1}, a good rate capability, an excellent cycling stability (99.5% after 20 000 cycles), and competitive energy density (36 W h kg^{-1} at a current density of 0.2 A g^{-1}) and power density (11 kW kg^{-1} at a current density of 50 A g^{-1}). In addition, DFT calculations were carried out to verify the formation of the core–shell structure during the spray-drying process which was corroborated by XPS chemical analyses and SEM and TEM characterization. The controllability and designability of the spray-drying process indicate that it might be a universal strategy to synthesize core–shell particles with graphene or other 2D materials as the shell.

Conflicts of interest

There are no conflicts to declare.

Acknowledgements

This work was supported by the Natural Science Foundation of China (Grant No. 51772165) and the National Key R&D Program of China (Grant No. 2017YFB1103300).

Notes and references

1 K. S. Kumar, N. Choudhary, Y. Jung and J. Thomas, *ACS Energy Lett.*, 2018, **3**, 482–495.
2 S. K. Bhardwaj, N. Bhardwaj, R. Kaur, J. Mehta, A. L. Sharma, K. H. Kim and A. Deep, *J. Mater. Chem. A*, 2018, **6**, 14992–15009.
3 C. Liu, X. Yan, F. Hu, G. Gao, G. Wu and X. Yang, *Adv. Mater.*, 2018, **30**, e1705713.
4 S. Saha, S. Chhetri, P. Khanra, P. Samanta, H. Koo, N. C. Murmu and T. J. J. o. E. S. Kuila, *Journal of Energy Storage*, 2016, **6**, 22–31.
5 S. Faraji and F. N. Ani, *Renewable Sustainable Energy Rev.*, 2015, **42**, 823–834.
6 X. Li, Q. Song, L. Hao and L. Zhi, *Small*, 2014, **10**, 2122–2135.
7 A. Khosrozadeh, G. Singh, Q. Wang, G. X. Luo and M. Xing, *J. Mater. Chem. A*, 2018, **6**, 21064–21077.
8 X. C. Dong, H. Xu, X. W. Wang, Y. X. Huang, M. B. Chan-Park, H. Zhang, L. H. Wang, W. Huang and P. Chen, *ACS Nano*, 2012, **6**, 3206–3213.
9 K. Li, Y. Huang, J. Liu, M. Sarfraz, P. O. Agboola, I. Shakir and Y. Xu, *J. Mater. Chem. A*, 2018, **6**, 1802–1808.
10 X. X. Sun, P. Cheng, H. J. Wang, H. Xu, L. Q. Dang, Z. H. Liu and Z. B. Lei, *Carbon*, 2015, **92**, 1–10.
11 Z. N. Li, S. Gadipelli, Y. C. Yang and Z. X. Guo, *Small*, 2017, **13**, 1702474.
12 J. Azadmanjiri, V. K. Srivastava, P. Kumar, M. Nikzad, J. Wang and A. M. Yu, *J. Mater. Chem. A*, 2018, **6**, 702–734.
13 E. Kim, H. Kim, B. J. Park, Y. H. Han, J. H. Park, J. Cho, S. S. Lee and J. G. Son, *Small*, 2018, **14**, e1704209.
14 D. Parviz, S. D. Metzler, S. Das, F. Irin and M. J. Green, *Small*, 2015, **11**, 2661–2668.
15 N. Castro, V. Durrieu, C. Raynaud and A. Rouilly, *Carbohydr. Polym.*, 2016, **144**, 464–473.
16 Y. L. Huang, Q. M. Gong, Q. Zhang, Y. Shao, J. J. Wang, Y. Q. Jiang, M. Zhao, D. M. Zhuang and J. Liang, *Nanoscale*, 2017, **9**, 2340–2347.
17 X. R. Wen, D. S. Zhang, T. T. Yan, J. P. Zhang and L. Y. Shi, *J. Mater. Chem. A*, 2013, **1**, 12334–12344.
18 W. Xia, Y. Wang, R. Bergstrasser, S. Kundu and M. Muhler, *Appl. Surf. Sci.*, 2007, **254**, 247–250.
19 K. A. Wepasnick, B. A. Smith, K. E. Schrote, H. K. Wilson, S. R. Diegelmann and D. H. Fairbrother, *Carbon*, 2011, **49**, 24–36.
20 Z. J. Tang, Z. X. Pei, Z. F. Wang, H. F. Li, J. Zeng, Z. H. Ruan, Y. Huang, M. S. Zhu, Q. Xue, J. Yu and C. Y. Zhi, *Carbon*, 2018, **130**, 532–543.
21 W. J. Qian, F. X. Sun, Y. H. Xu, L. H. Qiu, C. H. Liu, S. D. Wang and F. Yan, *Energy Environ. Sci.*, 2014, **7**, 379–386.
22 Z. Li, S. Gadipelli, Y. Yang and Z. Guo, *Small*, 2017, **13**, 1702474.
23 B. Xu, H. Duan, M. Chu, G. P. Cao and Y. S. Yang, *J. Mater. Chem. A*, 2013, **1**, 4565–4570.
24 Y. Chen, X. Zhang, H. Zhang, X. Sun, D. Zhang and Y. Ma, *RSC Adv.*, 2012, **2**, 7747–7753.
25 W. Qian, J. Yan, Y. Wang, W. Tong, M. Zhang, X. Jing and Z. Fan, *Carbon*, 2014, **67**, 119–127.
26 Y. Y. Yin, R. Y. Li, Z. J. Li, J. K. Liu, Z. G. Gu and G. L. Wang, *Electrochim. Acta*, 2014, **125**, 330–337.
27 Z. Chao, X. Zhou, H. Cao, G. Wang and Z. Liu, *J. Power Sources*, 2014, **258**, 290–296.
28 G. Q. Zu, J. Shen, L. P. Zou, F. Wang, X. D. Wang, Y. W. Zhang and X. D. Yao, *Carbon*, 2016, **99**, 203–211.
29 Y. Zhong, T. Shi, Y. Huang, S. Cheng, G. Liao and Z. Tang, *Electrochim. Acta*, 2018, **269**, 676–685.
30 R. T. Woodward, F. Markoulidis, F. De Luca, D. B. Anthony, D. Malko, T. O. McDonald, M. S. P. Shaffer and A. Bismarck, *J. Mater. Chem. A*, 2018, **6**, 1840–1849.
31 V. Strauss, K. Marsh, M. D. Kowal, M. El-Kady and R. B. Kaner, *Adv. Mater.*, 2018, 30.
32 P. Simon and Y. Gogotsi, *Nat. Mater.*, 2008, **7**, 845–854.
33 Y. L. Huang, Y. Zhao, Q. M. Gong, M. Y. Weng, J. F. Bai, X. Liu, Y. Q. Jiang, J. J. Wang, D. Z. Wang, Y. Shao, M. Zhao, D. M. Zhuang and J. Liang, *Electrochim. Acta*, 2017, **228**, 214–225.
34 X. H. Cao, Y. M. Shi, W. H. Shi, G. Lu, X. Huang, Q. Y. Yan, Q. C. Zhang and H. Zhang, *Small*, 2011, **7**, 3163–3168.
35 M. Yang, Y. R. Zhong, J. Bao, X. L. Zhou, J. P. Wei and Z. Zhou, *J. Mater. Chem. A*, 2015, **3**, 11387–11394.
36 J. Kim, J. H. Jeon, H. J. Kim, H. Lim and I. K. Oh, *ACS Nano*, 2014, **8**, 2986–2997.
37 O. Leenaerts, B. Partoens and F. M. Peeters, *Phys. Rev. B: Condens. Matter Mater. Phys.*, 2009, **79**, 235440.

38 G. X. Wang, B. Wang, J. Park, J. Yang, X. P. Shen and J. Yao, *Carbon*, 2009, **47**, 68–72.
39 A. M. Puziy, O. I. Poddubnaya, B. Gawdzik and M. Sobiesiak, *Adsorption*, 2016, **22**, 459–464.
40 R. A. Fonseca-Correa, L. Giraldo and J. C. Moreno-Pirajan, *Microporous Mesoporous Mater.*, 2017, **248**, 164–172.
41 X. Liang, Y. Guo, Q. U. Deyu, B. Deng, H. Liu and D. Tang, *J. Power Sources*, 2013, **225**, 286–292.
42 A. Anson, J. Jagiello, J. B. Parra, M. L. Sanjuan, A. M. Benito, W. K. Maser and M. T. Martinez, *J. Phys. Chem. B*, 2004, **108**, 15820–15826.
43 J. P. Perdew and M. Levy, *Phys. Rev. Lett.*, 1983, **51**, 1884–1887.
44 P. Yan, J. Zheng, J. Zheng, Z. Wang, G. Teng, S. Kuppan, J. Xiao, G. Chen, F. Pan and J. G. J. A. E. M. Zhang, *Adv. Energy Mater.*, 2016, **6**, 1502455.
45 J. Yang, J. Hu, M. Weng, R. Tan, L. Tian, J. Yang, J. Amine, J. Zheng, H. Chen and F. Pan, *ACS Appl. Mater. Interfaces*, 2017, **9**, 4587–4596.
46 L. L. Tian, J. Yang, M. Y. Weng, R. Tan, J. X. Zheng, H. B. Chen, Q. C. Zhuang, L. M. Dai and F. Pan, *ACS Appl. Mater. Interfaces*, 2017, **9**, 7125–7130.
47 M. F. Craciun, I. Khrapach, M. D. Barnes and S. Russo, *J. Phys.: Condens. Matter*, 2013, **25**, 423201.
48 G. Xie, R. Yang, P. Chen, J. Zhang, X. Tian, S. Wu, J. Zhao, M. Cheng, W. Yang, D. Wang, C. He, X. Bai, D. Shi and G. Zhang, *Small*, 2014, **10**, 2280–2284.
49 M. M. Yan, Q. G. Jiang, T. Zhang, J. Y. Wang, L. Yang, Z. Y. Lu, H. Y. He, Y. S. Fu, X. Wang and H. J. Huang, *J. Mater. Chem. A*, 2018, **6**, 18165–18172.
50 J. Chen, Y. R. Li, L. Huang, C. Li and G. Q. Shi, *Carbon*, 2015, **81**, 826–834.
51 H. Peisert, T. Chasse, P. Streubel, A. Meisel and R. Szargan, *J. Electron Spectrosc. Relat. Phenom.*, 1994, **68**, 321–328.
52 C. P. Hunt, M. T. Anthony and M. P. Seah, *Surf. Interface Anal.*, 1984, **6**, 92–93.
53 S. Y. Yin, Z. Q. Niu and X. D. Chen, *Small*, 2012, **8**, 2458–2463.
54 X. M. Feng, Z. Z. Yan, N. N. Chen, Y. Zhang, Y. W. Ma, X. F. Liu, Q. L. Fan, L. H. Wang and W. Huang, *J. Mater. Chem. A*, 2013, **1**, 12818–12825.
55 Y. L. Huang, Q. M. Gong, Q. Zhang, Y. Shao, J. J. Wang, Y. Q. Jiang, M. Zhao, D. M. Zhuang and J. Liang, *Nanoscale*, 2017, **9**, 2340–2347.
56 J. Yan, L. Li and C. O'Grady, *Comput. Phys. Commun.*, 2013, **184**, 2728–2733.
57 W. L. Jia, J. Y. Fu, Z. Y. Cao, L. Wang, X. B. Chi, W. G. Gao and L. W. Wange, *J. Comput. Phys.*, 2013, **251**, 102–115.
58 S. Grimme, *J. Comput. Chem.*, 2006, **27**, 1787–1799.
59 D. J. Chadi, *Phys. Rev. B: Solid State*, 1977, **16**, 1746–1747.
60 D. R. Hamann, *Phys. Rev. B*, 2013, **88**, 085117.
61 M. Schlipf and F. Gygi, *Comput. Phys. Commun.*, 2015, **196**, 36–44.